Journal of Colloid and Interface Science 360 (2011) 262–271

Contents lists available at ScienceDirect

Journal of Colloid and Interface Science

www.elsevier.com/locate/jcis

Streaming current and wall dissolution over 48 h in silica nanochannels

Mathias Bækbo Andersen [a,*], Henrik Bruus [a], Jaydeep P. Bardhan [b], Sumita Pennathur [c]

[a] Department of Micro- and Nanotechnology, Technical University of Denmark, DTU Nanotech Building 345 East, DK-2800 Kongens Lyngby, Denmark
[b] Department of Molecular Biophysics and Physiology, Rush University Medical Center, Chicago, IL 60612, USA
[c] Department of Mechanical Engineering, University of California, Santa Barbara, CA 93106, USA

ARTICLE INFO

Article history:
Received 30 November 2010
Accepted 7 April 2011
Available online 16 April 2011

Keywords:
Nanofluidics
Silica dissolution
Gouy–Chapman–Stern model
Streaming current
Cyanosilane surface coating

ABSTRACT

We present theoretical and experimental studies of the streaming current induced by a pressure-driven flow in long, straight, electrolyte-filled nanochannels. The theoretical work builds on our recent one-dimensional model of electro-osmotic and capillary flow, which self-consistently treats both the ion concentration profiles, via the nonlinear Poisson–Boltzmann equation, and the chemical reactions in the bulk electrolyte and at the solid–liquid interface. We extend this model to two dimensions and validate it against experimental data for electro-osmosis and pressure-driven flows, using eight 1-μm-wide nanochannels of heights varying from 40 nm to 2000 nm. We furthermore vary the electrolyte composition using KCl and borate salts, and the wall coating using 3-cyanopropyldimethylchlorosilane. We find good agreement between prediction and experiment using literature values for all parameters of the model, i.e., chemical reaction constants and Stern-layer capacitances. Finally, by combining model predictions with measurements over 48 h of the streaming currents, we develop a method to estimate the dissolution rate of the silica walls, typically around 0.01 mg/m^2/h, equal to 45 pm/h or 40 nm/yr, under controlled experimental conditions.

1. Introduction

Advances in nanofabrication technology promise to allow the emergence of nanofluidic devices as enabling technologies in a diverse set of emerging applications, including pharmaceuticals, environmental health and safety, and bioanalytical systems. Nanoscale coupling of surface chemistry, electrokinetics, and fluid dynamics provides a rich set of phenomena not available in larger devices, which in turn allow nanofluidic systems to offer novel functional capabilities. To fully exploit the potential of nanofluidics, a detailed understanding of electrokinetic phenomena is thus required including the distributions of ions in electrical double layers, surface charge effects, and electric potential effects on the fluid [1–5].

Because fused silica is one of the most prevalent materials used to fabricate nanochannels, its behavior in electrolyte solutions is particularly important and has received much specialized attention. Two important aspects pertaining to the use of silica for nanosystems are deterioration due to dissolution [6–9] and the effects induced by corners in channels where a full 2D modeling of the channel cross section is necessary rather than the usual planar 1D approximation [10–13].

Regarding the dissolution rate, it is important to determine whether dissolution of silica is significant when it is used to confine electrolytes in nanometer-sized channels. For example, Greene et al. [9] studied the dissolution rates in systems of electrolytes in nanometer-sized confinement under pressure between quartz (SiO_2) and mica. They found that the dissolution rate of quartz initially is 1–4 nm/min and that this drops over several hours to a constant rate around 0.01 nm/min or 5 μm/yr. Such rates might influence the long-term stability and operability of silica nanofluidic devices, and devising ways to inhibit such dissolution phenomena, by surface coatings [14], is therefore important.

Regarding 2D corner effects in pressure-driven flows in nanometer-sized geometries, some studies involved complex or poorly defined networks of nanochannels, such as those found in porous glass [15], columns packed with latex beads [16], and sandstone cores [17], while other studies on desalination [18–20] and energy conversion [15,21–24] involved geometries where simpler 1D models sufficed. In the latter studies, streaming currents were measured in individual rectangular silica nanochannels as functions of varying pressure, channel height, as well as salt concentration. Good agreement was obtained between measurements and predictions from different 1D models for the electrostatic properties of the surface, including chemical-equilibrium models. The 1D planar-wall chemical-equilibrium model has proved successful in several other studies [25–28]. Recently, we extended the chemical-equilibrium model to allow surface-related parameters, such

* Corresponding author.
E-mail address: mathias.andersen@nanotech.dtu.dk (M.B. Andersen).

0021-9797/$ - see front matter © 2011 Elsevier Inc. All rights reserved.
doi:10.1016/j.jcis.2011.04.011

as Stern-layer capacitance C_s and the surface equilibrium pK_a constants, to vary with the composition of the solid-liquid interface and validated it experimentally by both capillary filling methods and electrokinetic current monitoring [14,29]. However, as rectangular nanochannels with low aspect ratios are now readily fabricated and operated with significant overlap of the electric double layer, as in this work and by others [10–13], it is relevant to study how the presence of side walls and corners affects the electrokinetics of chemical-equilibrium models.

The structure of the paper is as follows. We present our theoretical 2D model in Section 2 and describe its numerical implementation along with a theoretical 1D–2D modeling comparison in Section 3. In contrast to our previous work [14,29], this model contains no adjustable parameters. We validate our model by comparing predicted values of electro-osmotic flow velocity and of streaming currents to those measured in eight different bare and cyanosilane-coated nanochannels with depths ranging nominally between 40 nm and 2000 nm. The experimental setup and procedure are described in Section 4, while the theoretical and experimental results are presented and discussed in Section 5. At the end of Section 5, we combine model prediction with 48 h of streaming current measurements to estimate the dissolution rate of the silica walls under controlled experimental conditions. We end with concluding remarks in Section 6.

2. Theory

Theoretical modeling of ionic transport in nanochannels is traditionally based on three components: the Gouy–Chapman–Stern model of electrostatic screening, a position-independent boundary condition at the wall (either given potential, given surface charge, or equilibrium deprotonation reactions [25–28,30,31,14,29]), and continuum fluid dynamics equations [32,33,21–24,34,5,29]. In the present work, we extend the prior chemical-equilibrium modeling by allowing the surface charge, potential and pH (the concentration of the hydronium ion H^+) to vary with position along the surface through a full 2D modeling of the channel cross section. The bulk pH is a function of the composition of the electrolyte, and the entire bulk chemistry is modeled using chemical-equilibrium acid–base reactions described in Section 2.1; the physical parameters used in our model are listed in Table 1. After solving the nonlinear electrostatic Poisson–Boltzmann equation in the full 2D cross-sectional geometry, we determine the electro-osmotic flow or the streaming current arising in the system by applying an external electrical potential drop or a pressure drop along the channel, respectively.

Our extended 2D electrokinetic chemical-equilibrium model thus consists of four parts: (*i*) chemical reactions in the bulk, which determine the concentrations of the ions in our electrolyte $[H^+, OH^-, HCO_3^-, CO_3^{2-}, K^+, Cl^-, Na^+, B(OH)_4^-]$, (*ii*) chemical reactions at the surface, which determine the electric potential and charge of the bare or coated silica surface, (*iii*) the 2D Poisson–Boltzmann equation for the electrical potential combining the first two parts, and (*iv*) the 2D Stokes equation including external force densities from the externally applied drop along the channel in pressure or electrical potential. We solve parts (*i*)–(*iii*) self-consistently and then insert the resulting distributions of charged species in part (*iv*) to calculate the flow velocity and the current density. The silica wall is sketched in Fig. 1.

Table 1
Basic physical parameters used in our model.

Quantity	Symbol	Value	Unit
Temperature	T	296	K
Viscosity, electrolyte solution	η	930	μPa s
Permittivity, electrolyte solution	ε	691	pF m^{-1}
Length of nanochannel	L	20	mm
Stern capacitance, bare silica[a]	C_s	0.3	F m^{-2}
Stern capacitance, coated silica[b]	C_s	0.2	F m^{-2}
Surface site density, bare silica [c]	Γ	5.0	nm^{-2}
Surface site density, coated silica [d]	Γ	3.8	nm^{-2}

[a] From Ref. [21].
[b] From Refs. [35,14,29].
[c] From Refs. [35–37,27,29].
[d] From Ref. [38].

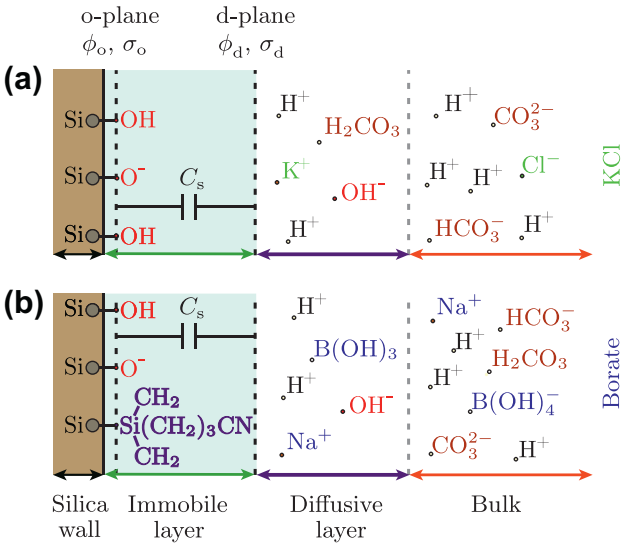

Fig. 1. (a) Sketch of a silica wall (brown) and its Stern layer (blue), with surface capacitance C_s, in contact with an aqueous KCl solution. The four regions of main interest are identified as: the silica wall, the immobile Stern layer, the diffusive layer, and the bulk. The dashed vertical line denoted "o-plane" is where the bound surface charge σ_o resides, while the dashed black line denoted "d-plane" marks the beginning of the diffuse, mobile layer, a layer stretching from the d-plane to the bulk, and in which a mobile screening charge per area $\sigma_d = -\sigma_o$ resides. The electrical potential at the o- and d-plane is denoted ϕ_o and ϕ_d, respectively. (b) Same as panel (a) except now for an electrolyte containing sodium borate ions. Also indicated is a surface coating of cyanosilane $Si(CH_2)_5CN$ molecules. C_s is constant along the surface, while σ_o and ϕ_o vary. (For interpretation of the references to color in this figure legend, the reader is referred to the web version of this article.)

2.1. Bulk chemistry

As in our previous work [14,29], we calculate all bulk ionic concentrations of the reservoirs using the method of "chemical families" [39,40]. Briefly, this approach provides a simple, yet powerful means to manage the book-keeping associated with modeling multiple protonatable species. For example, the chemical family for H_2CO_3 has three members: the fully protonated H_2CO_3 (valence 0), the singly deprotonated HCO_3^- (valence −1), and the doubly deprotonated HCO_3^{-2} (valence −2). We define the limits for the valence z_X of a chemical family X as $n_X \leqslant z_X \leqslant p_X$, so here $n_X = -2$ and $p_X = 0$. The chemical families relevant for this work, the associated dissociation reactions, and the reaction constants pK_{X,z_X} are listed in Table 2. We next employ two assumptions about the bulk solutions in the reservoirs: the total concentration c_X^{tot} of every chemical family is known, and the bulk solution is homogeneous and electrically neutral. This allows us to calculate the bulk concentrations c^b_{X,z_X} from the equations

$$K_{X,z_X} c^b_{X,z_X+1} = c^b_{X,z_X} c^b_H, \quad \text{dissociation reactions}, \tag{1a}$$

$$\sum_{z_X=n_X}^{p_X} c^b_{X,z_X} = c^{tot}_X, \quad \text{conservation of mass}, \tag{1b}$$

$$\sum_{X,z_X} z_X c^b_{X,z_X} = 0, \quad \text{charge neutrality}, \tag{1c}$$

Table 2
List of the chemical families X used in this work together with charge states z_X, the associated reaction schemes, and reaction constants $pK_{X,z_X} = -\log_{10}(K_X, z_X/1\ M)$. Note that the pK_{X,z_X} values are for dissociation processes. The silanol family involves surface reactions, while all other families involve bulk reactions.

Chemical family X	z_X	Reaction scheme (dissociation)		pK_{X,z_X}
Potassium	0	KOH		–
hydroxide	+1	KOH	$\rightleftharpoons K^+ + OH^-$	14.00 [a]
Sodium	0	NaOH		–
hydroxide	+1	NaOH	$\rightleftharpoons Na^+ + OH^-$	14.00 [a]
Hydrochloric	0	HCl		–
acid	−1	HCl	$\rightleftharpoons Cl^- + H^+$	−7.00 [a]
Boric	0	$HB(OH)_4$		–
acid	+1	$HB(OH)_4$	$\rightleftharpoons B(OH)_4^- + H^+$	9.24 [a]
Carbonic	0	H_2CO_3		–
acid	−1	H_2CO_3	$\rightleftharpoons HCO_3^- + H^+$	6.35[a]
	−2	HCO_3^-	$\rightleftharpoons CO_3^{2-} + H^+$	10.33[a]
Water	0	H_2O		
	±1[b]	H_2O	$\rightleftharpoons OH^- + H^+$	14.00
Silanol	0	SiOH		–
	−1	SiOH	$\rightleftharpoons SiO^- + H^+$	6.6 ±0.6 [c]

[a] From Ref. [41] at 25 °C.
[b] For sum over OH^- and H^+ ions see the remark after Eq. (1c).
[c] From Refs. [42,25,31,43,27,29].

where c_H^b is the bulk concentration of hydronium ions. Note that the index z_X includes neither H^+ nor OH^- for any family X, except for water where z_X includes both H^+ and OH^-. A more detailed account of the reactions is given in the Supplementary information.

Once the bulk concentrations c^b_{X,z_X} are known, two parameters characterizing the electrolyte can be determined: the ionic strength c_I and the Debye screening length λ_D,

$$c_I = \frac{1}{2}\sum_{X,z_X}(z_X)^2 c^b_{X,z_X}, \tag{2a}$$

$$\lambda_D = \left[\frac{\epsilon k_B T}{2e^2 c_I}\right]^{\frac{1}{2}}. \tag{2b}$$

The two ionic strengths used in this work are c_I = 1 mM and 20 mM, for which $\lambda_D \approx 10$ nm and 2 nm, respectively.

2.2. Surface chemistry

In Fig. 1 is shown a sketch of the interface between the silica wall and the electrolyte. We model the solid/liquid interface in three parts [14]: the silanol surface (the "o-surface" with surface charge σ_o and potential ϕ_o), the electrically charged, diffusive screening layer (extending a few times the Debye length λ_D from the "d-surface" and having space charge per area σ_d and zeta potential ϕ_d), and the immobile Stern layer in between having capacitance per unit area C_s. For bare silica surfaces, we use C_s = 0.3 F m^{-2} [21], and for cyanosilane-coated silica, we use C_s = 0.2 F m^{-2} consistent with Ref. [14].

For the pH range relevant in this work, deprotonation of silica is the only important surface reaction, making SiOH and SiO^- the only significant surface groups, and the corresponding equilibrium equation is,

$$SiOH \rightleftharpoons SiO^- + H_o^+, \tag{3a}$$

$$10^{-pK}\Gamma_{SiOH} = \Gamma_{SiO^-} c_H^o, \tag{3b}$$

where H_o^+ is a hydronium ion at the o-surface, Γ_i is the surface site density of surface group i, c_H^o is the concentration of hydronium ions at the o-surface, and pK = 6.6 ± 0.6 [42,25,31,43,27,29], see Table 2. The sum of the site densities equals the known total site density Γ [36,37,35,27,29,38],

$$\Gamma_{SiOH} + \Gamma_{SiO^-} = \Gamma = \begin{cases} 5.0\ nm^{-2}, & \text{bare silica,} \\ 3.8\ nm^{-2}, & \text{coated silica,} \end{cases} \tag{4}$$

and the surface charge is given by the site density of negative surface groups as

$$\sigma_o = -e\Gamma_{SiO^-}. \tag{5}$$

Assuming a Boltzmann distribution of ions, we obtain

$$c_H^o = c_H^b \exp\left(-\frac{e}{k_B T}\phi_o\right), \tag{6}$$

and the usual linear capacitor model of the immobile Stern layer becomes

$$C_s(\phi_o - \phi_d) = \sigma_o. \tag{7}$$

Finally, the diffuse-layer potential ϕ_d can be expressed in terms of the surface charge σ_o [25] by combining Eqs. (3b)–(7)

$$\phi_d(\sigma_o) = \frac{k_B T}{e}\left[\ln\left(\frac{-\sigma_o}{e\Gamma + \sigma_o}\right) - \frac{pH_b - pK}{\log_{10}(e)}\right] - \frac{\sigma_o}{C_s}, \tag{8}$$

where $pH_b = -\log_{10}(c_H^b/1\ M)$. This equation constitutes a nonlinear mixed boundary condition for the 2D Poisson–Boltzmann equation described in the following section.

2.3. Electrohydrodynamics in the 2D channel cross section

Much work in nanochannels has involved very large width-to-height ratios making a 1D approximation valid. However, for smaller aspect ratios, this approximation breaks down and a full 2D treatment of the channel cross section should at least be checked. Here, we set out to investigate the model predictions from such a 2D treatment using the chemical-equilibrium surface charge model of the previous section. For the experimental systems of interest in this work, the aspect ratio of the rectangular nanochannels ranges from 27 to 0.5, and in some cases involve overlapping or nearly overlapping electrical double layers, see Section 4. We verify our theoretical model by comparing the predictions with two independent sets of measurements: electro-osmotically driven flow and pressure-generated streaming currents.

For a straight nanochannel of length L along the x-axis, width w along the y-axis, and height $2h$ along the z-axis, the domain of interest is the 2D cross-sectional geometry of the nanochannel parallel to the yz-plane. The electrohydrodynamics of the electrolyte is governed by the Poisson–Boltzmann equation of the electric potential $\phi(y,z)$ coupled to the Stokes equation of the axial velocity field $u(y,z)$. The electric potential obeys the Poisson equation

$$-\epsilon\nabla^2\phi(y,z) = \rho_{el}(y,z), \tag{9}$$

where ρ_{el} is the electric charge density, which for Boltzmann-distributed ions is given by

$$\rho_{el}(y,z) = e\sum_X \sum_{z_X = n_X}^{p_X} z_X c^b_{X,z_X}(y,z)\exp\left[-\frac{z_X e\phi(y,z)}{k_B T}\right]. \tag{10}$$

Together, Eqs. (9) and (10) form the Poisson–Boltzmann equation. The nonlinear, mixed boundary condition for ϕ is

$$\boldsymbol{n}\cdot\nabla\phi = -\frac{1}{\epsilon}\sigma_o(\phi_d), \quad \text{at the d-surface}, \tag{11}$$

where $\boldsymbol{n}$ is the surface normal vector pointing into the electrolyte. Together with Eq. (8) this constitutes a mixed nonlinear boundary condition which can be neatly implemented using the weak form, finite element modeling formalism in COMSOL as described in the Supplementary information.

The Reynolds number for the flow of the electrolyte in the long, straight nanochannel is much smaller than unity, so the velocity

field is governed by the Stokes equation with a body-force density. From symmetry considerations, it follows that only the axial velocity component is non-zero and depends only on the transverse coordinates. In this work, the flow is either purely electro-osmotically driven or purely pressure driven, and the resulting velocity field is denoted u_{eo} and u_p, respectively. The Stokes equation for the two cases becomes

$$\nabla^2 u_{eo}(y,z) = -\rho_{el}(y,z)\frac{\Delta V}{\eta L}, \tag{12a}$$

$$\nabla^2 u_p(y,z) = -\frac{\Delta p}{\eta L}, \tag{12b}$$

where we have assumed that the gradients along x in the electric potential and in the pressure, due to the applied potential difference ΔV and applied pressure difference Δp, respectively, are constant. For both velocity fields, the usual no-slip boundary condition applies at the wall (the d-surface)

$$u_{eo} = u_p = 0, \quad \text{at the d-surface.} \tag{13}$$

Note that in our model the electric and hydrodynamic fields ϕ and u are only coupled in the electro-osmotic case, Eq. (12a).

Once the electric charge density $\rho_{el}(y,z)$, the electro-osmotically driven velocity field $u_{eo}(y,z)$, and the pressure-driven flow velocity $u_p(y,z)$ have been determined, the area-averaged electro-osmotic flow velocity $\langle u_{eo}\rangle$ and the streaming current I_p can be found as

$$\langle u_{eo}\rangle = \frac{1}{hw}\int_0^w \mathrm{d}y \int_0^h \mathrm{d}z\, u_{eo}(y,z), \tag{14a}$$

$$I_p = 2\int_0^w \mathrm{d}y \int_0^h \mathrm{d}z\, \rho_{el}(y,z)u_p(y,z). \tag{14b}$$

2.4. Non-dimensionalization

To facilitate our numerical implementation, we non-dimensionalize our equations. We introduce the thermal voltage ϕ_T, the velocity scale u_o, the capacitance scale C_o, and the streaming current scale I_p^o

$$\phi_T = \frac{k_B T}{e}, \quad u_o = \frac{\lambda_D^2 \Delta p}{\eta L}, \tag{15a}$$

$$C_o = \frac{e^2 \Gamma}{k_B T}, \quad I_p^o = e c_I \frac{\lambda_D^4 \Delta p}{\eta L}. \tag{15b}$$

Grouping quantities with dimension of length $\boldsymbol{r} = \{y,z,h,w\}$, we define our dimensionless quantities, denoted by a tilde, as

$$\tilde{\boldsymbol{r}} = \frac{\boldsymbol{r}}{\lambda_D}, \quad \tilde{u} = \frac{u}{u_o}, \quad \tilde{C}_s = \frac{C_s}{C_o}, \quad \tilde{C}_{dl} = \frac{C_{dl}}{C_o}, \tag{16a}$$

$$\tilde{\phi}_d = \frac{\phi_d}{\phi_T}, \quad \tilde{\sigma}_o = \frac{\sigma_o}{e\Gamma}, \quad \tilde{\rho}_{el} = \frac{\rho_{el}}{e c_I}, \quad \tilde{I}_p = \frac{I_p}{I_p^o}, \tag{16b}$$

where $C_{dl} = \epsilon/\lambda_D$ is the low-voltage diffuse-layer capacitance. As we are especially interested in the effects occurring when the electric double-layers overlap, λ_D is chosen as normalization for the length scales. The non-dimensionalized governing equations become

$$\tilde{\nabla}^2\tilde{\phi}(\tilde{y},\tilde{z}) = -\frac{1}{2}\tilde{\rho}_{el}(\tilde{y},\tilde{z}), \tag{17a}$$

$$\tilde{\nabla}^2\tilde{u}_{eo}(\tilde{y},\tilde{z}) = -\chi\tilde{\rho}_{el}(\tilde{y},\tilde{z}), \tag{17b}$$

$$\tilde{\nabla}^2\tilde{u}_p(\tilde{y},\tilde{z}) = -1, \tag{17c}$$

where $\chi = c_I e\Delta V/\Delta p$ is the dimensionless electrohydrodynamic coupling constant. The corresponding dimensionless boundary conditions at the d-surface are

$$\tilde{\phi}_d = \ln\left(\frac{-\tilde{\sigma}_o}{1+\tilde{\sigma}_o}\right) - \frac{\mathrm{pH}_b - \mathrm{p}K}{\log_{10}(\mathrm{e})} - \frac{\tilde{\sigma}_o}{\tilde{C}_s}, \tag{18a}$$

$$\boldsymbol{n}\cdot\tilde{\nabla}\tilde{\phi} = -\frac{\tilde{\sigma}_o}{\tilde{C}_{dl}}, \tag{18b}$$

$$\tilde{u}_{eo} = \tilde{u}_p = 0. \tag{18c}$$

The non-dimensionalized area-averaged electro-osmotic velocity and streaming current $\tilde{I}_p$ become

$$\langle\tilde{u}_{eo}\rangle = \frac{1}{\tilde{h}\tilde{w}}\int_0^{\tilde{w}} \mathrm{d}\tilde{y} \int_0^{\tilde{h}} \mathrm{d}\tilde{z}\, \tilde{u}_{eo}(\tilde{y},\tilde{z}), \tag{19a}$$

$$\tilde{I}_p = 2\int_0^{\tilde{w}} \mathrm{d}\tilde{y} \int_0^{\tilde{h}} \mathrm{d}\tilde{z}\, \tilde{\rho}_{el}(\tilde{y},\tilde{z})\tilde{u}_p(\tilde{y},\tilde{z}). \tag{19b}$$

3. Numerical simulation

Numerical simulations are performed using the finite-element-method software COMSOL combined with Matlab by implementing in 2D the dimensionless coupled equations of Section 2.4. The nonlinear, mixed boundary condition Eqs. (18a) and (18b) for the electrostatic problem is conveniently implemented using the method of Lagrange multipliers as described in the Supplementary information.

Due to the two symmetry lines of the rectangular cross section, we only consider the lower left quarter of the channel cross section. At the symmetry lines, we apply standard symmetry boundary conditions

$$\boldsymbol{n}\cdot\tilde{\nabla}\tilde{\phi} = 0, \tag{20a}$$

$$\boldsymbol{n}\cdot\tilde{\nabla}\tilde{u}_{eo} = 0, \tag{20b}$$

$$\boldsymbol{n}\cdot\tilde{\nabla}\tilde{u}_p = 0. \tag{20c}$$

To avoid numerical convergence problems near the corners of the cross section and to mimic fabrication resolution, we represent the corners by 1-nm-radius quarter circles.

The simulation accuracy has been checked in several ways. For very large aspect ratios, the 2D results agree well with those ob-

Table 3
The cross-sectional geometry of the eight different 20-mm-long channels used in experiments: average width w (±standard deviation Δw), average height $2h$ (±standard deviation Δh), aspect ratio $w/(2h)$, dimensionless channel half-height $\tilde{h} = h/\lambda_D$, and relative deviation in the streaming current between 1D and 2D modeling $\delta_{1D,2D}$. $\tilde{h}$ and $\delta_{1D,2D}$ are listed for the 1 mM KCl solution (pH 5.6 and λ_D = 10 nm) and for the 10 mM borate buffer (pH 9.24 and λ_D = 2 nm).

#	$w \pm \Delta w$ (nm) width	$2h \pm \Delta h$ (nm) height	$w/(2h)$ aspect ratio	$\tilde{h}$ KCl 1 mM	$\delta_{1D,2D}$ KCl (%)	$\tilde{h}$ borate 10 mM	$\delta_{1D,2D}$ borate (%)
1	1043 ± 100	38.6 ± 0.6	27.0	2.0	1.0	10	0.3
2	1090 ± 100	68.8 ± 0.8	15.0	3.6	1.3	16	0.3
3	1113 ± 100	82.5 ± 0.5	13.5	4.3	1.3	19	0.3
4	1118 ± 100	103 ± 0.6	10.9	5.4	1.4	24	0.3
5	1021 ± 100	251 ± 0.8	4.1	13	1.6	59	0.4
6	1099 ± 100	561 ± 1.0	2.0	29	1.6	131	0.3
7	1181 ± 100	1047 ± 2.0	1.1	55	1.5	245	0.3
8	1067 ± 100	2032 ± 2.0	0.5	106	1.7	475	0.4

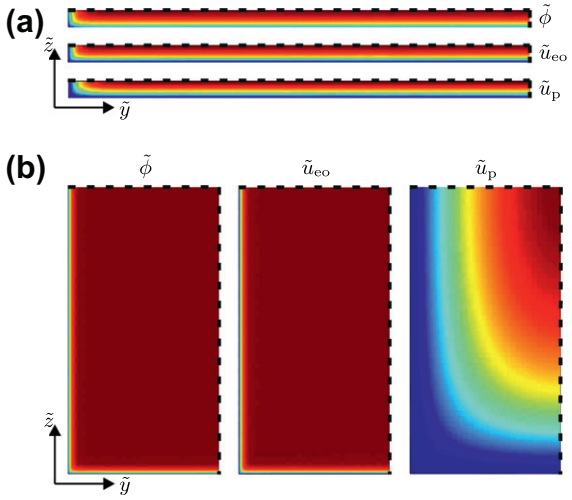

Fig. 2. Color plots (blue = zero, red = maximum) of calculated electric potential $\tilde{\phi}(\tilde{y},\tilde{z})$, electro-osmotic flow velocity $\tilde{u}_{eo}(\tilde{y},\tilde{z})$, and pressure-driven flow velocity $\tilde{u}_p(\tilde{y},\tilde{z})$ in the lower left corner of the rectangular nanochannel cross section. Full lines are the silica walls, while dashed lines are symmetry lines. Parameters correspond to the case of an aqueous 1 mM KCl solution (pH 5.6 and $\lambda_D \simeq 10$ nm) in bare silica channels (C_s = 0.3 F m^{-2}, Γ = 5.0 nm^{-2}, and pK = 6.6). (a) The shallowest channel used in our study; channel #1 in Table 3 with $w/(2h)$ = 27 and $\tilde{h} = 2$. (b) The tallest channel used in our study; channel #8 in Table 3 with $w/(2h)$ = 0.5 and $\tilde{h} = 106$. (For interpretation of the references to color in this figure legend, the reader is referred to the web version of this article.)

tained by a standard 1D method from the literature (data not shown). In addition, mesh convergence tests have been performed and show good convergence properties; an example is given in the Supplementary information of a plot of the calculated streaming current I_p as a function of the number of finite elements. Adequate convergence is achieved when employing more than a few thousand elements. Finally, by direct substitution of the computed solution, we have verified that the nonlinear, mixed boundary condition Eqs. (18a) and (18b) is obeyed. All tests we have performed support the claim that our predicted currents should be accurate to a relative error of 10^{-4} or better.

Qualitative color plots of calculated $\tilde{\phi}(\tilde{y},\tilde{z})$, $\tilde{u}_{eo}(\tilde{y},\tilde{z})$, and $\tilde{u}_p(\tilde{y},\tilde{z})$ are shown in Fig. 2 for the nanochannel cross sections having the largest and smallest aspect ratio, $w/(2h)$ = 27 in panel (a) and 0.5 in panel (b), respectively. Parameters correspond to the case of an aqueous 1 mM KCl solution (pH 5.6 and $\lambda_D \simeq 10$ nm) in bare silica channels (C_s = 0.3 F m^{-2}, Γ = 5.0 nm^{-2}, and pK = 6.6). In the shallow channel, panel (a), corresponding to channel #1 in Table 3 with $w/(2h)$ = 27 and $\tilde{h} = 2$, all three fields $\tilde{\phi}, \tilde{u}_{eo}$, and $\tilde{u}_p$, depend only on the z-coordinate except for the small edge region; thus, a 1D approximation is valid. In contrast, for smaller aspect ratio, see panel (b), corresponding to channel #8 in Table 3 with $w/(2h)$ = 0.5 and $\tilde{h} = 106$, only $\tilde{\phi}$ and $\tilde{u}_{eo}$ can locally be approximated by a 1D model, whereas this is clearly not the case for the pressure-driven velocity field $\tilde{u}_p$.

Furthermore, using our 2D model, we find that employing either constant-potential or constant-surface-charge boundary conditions is not accurate for small aspect-ratio channels. For the smallest channel height, $\tilde{h} = 2.0$, we plot in Fig. 3a the relative deviation for quantity f

$$\delta_{1D,2D} = \frac{f_{1D} - f_{2D}}{f_{2D}}, \tag{21}$$

of the locally varying value from the 2D model to that from a corresponding 1D model for the zeta potential ϕ_d (thick red curve) and

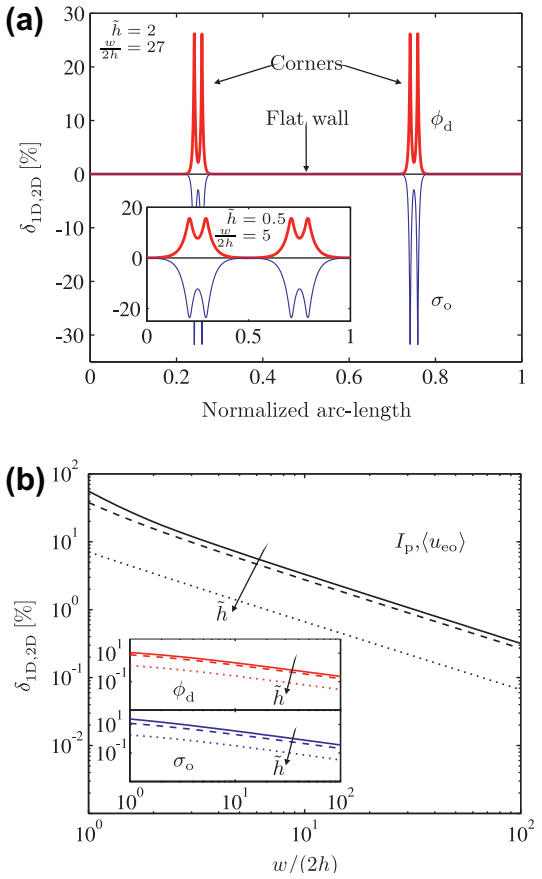

Fig. 3. The effect of corners calculated in 2D. (a) Relative deviation between the locally varying value from the 2D model and the constant value from a 1D model of the zeta potential ϕ_d (thick red curve) and surface charge σ_o (thin blue curve) versus the normalized arc-length along the d- and o-surface for channel #1 in Table 3 with 1 mM KCl, $\tilde{h} = 2$ and $w/(2h)$ = 27. The inset shows the case of $\tilde{h} = 0.5$ and $w/(2h)$ = 5. (b) Relative deviation of the value from the 2D model of the area-averaged electro-osmotic velocity $\langle u_{eo} \rangle$ (black), the streaming current I_p (black), the surface-average of ϕ_d (inset, blue), and the surface-average of σ_o (inset, red) to the corresponding values from a 1D model versus the aspect ratio $w/(2h)$ for $\tilde{h} = 0.5$ (full curves), $\tilde{h} = 2$ (dashed curves) and $\tilde{h} = 13$ (dotted curves). (For interpretation of the references to color in this figure legend, the reader is referred to the web version of this article.)

the surface charge σ_o (thin blue curve) along the normalized arc-length s of the d- and o-surfaces. This clearly shows the dependence of these variables on the position along the boundary of the 2D cross section: near the corners, the value of the potential increases about 25% and the surface charge drops about 30%. The inset in Fig. 3a shows the case with a higher degree of double-layer overlap, $\tilde{h} = 0.5$, and with smaller aspect ratio $w/(2h)$ = 5. Comparing the inset with the figure, it is clear that as the double-layer overlap becomes larger and the aspect ratio smaller 2D corner effects becomes increasingly significant as compared to a 1D model. We can therefore conclude that significant changes can be induced at corners in 2D domains in the chemical-equilibrium model. We now turn to look at how the combined effects from the equilibrium model and the presence of side-walls due to finite aspect-ratio geometries influence the difference between 1D and 2D modeling.

In Fig. 3b is shown a log-log plot of the relative deviation $\delta_{1D,2D}$ of the value from the 2D model of the area-averaged electro-osmotic velocity $\langle u_{eo} \rangle = \int_\Omega u_{eo}(y,z)\mathrm{d}A$ (black), the streaming current I_p (black), the surface-averaged zeta-potential $\int_{\partial\Omega} \phi_d \mathrm{d}s$ (inset, red), and the surface-averaged surface-charge $\int_{\partial\Omega} \sigma_o \mathrm{d}s$ (inset, blue) to the corresponding values from a 1D model as a function of the aspect ratio $w/(2h)$. Three different cases are shown: strong double-

layer overlap, $\tilde{h} = 0.5$ (full curves), moderate overlap, $\tilde{h} = 2.0$ (dashed curves, corresponding to channel #1 in Table 3), and no overlap, $\tilde{h} = 13$ (dotted curves, corresponding to channel #5 in Table 3). Large deviations are observed for the streaming current in channels with aspect ratio close to unity: $\delta_{1D,2D} = 56\%$ for $\tilde{h} = 0.5$, 38% for $\tilde{h} = 2$ and 7% for $\tilde{h} = 13$. We also note that as the aspect ratio increases, the relative deviation becomes smaller with a slope close to -1 in the log-log plot indicating that the relative deviation is inversely proportional to the aspect ratio. It is remarkable that the relative deviations for the area-averaged electro-osmotic flow velocity and the streaming current are nearly identical and that they therefore cannot be distinguished in Fig. 3b.

To obtain a significant deviation $\delta_{1D,2D}$ between the 1D and 2D models, the corner regions must be significant, and thus the aspect ratio must be low ($2h \approx w$) and the double layers must overlap ($\tilde{h} \approx 1$). Theoretically, this follows from the observations that the electrokinetic effects are governed by the smallest length scale λ_D and the 2D dependence of the velocity field is unimportant: for a smooth, cusp-less surface we denote the local normal and tangential coordinates relative to the surface by v and τ, respectively. Away from the corners, we have $\rho_{el}(v,\tau) \approx \rho_{el}(v)$, which decays on the small scale λ_D. Hence, by a Taylor expansion of the velocity around the no-slip value at the boundary, we obtain $\rho_{el}(v)u_p(v,\tau) \approx \rho_{el}(v)v\boldsymbol{n}\cdot\nabla u_p$. Neglecting corner effects (an error of the order $1/\tilde{h}$) and introducing $J_{\rho_{el}} = \int_0^\infty v\rho_{el}(v)\mathrm{d}v$, the streaming current can therefore be written as

$$I_p = \int_\Omega \rho_{el}u_p \mathrm{d}v\mathrm{d}\tau \approx J_{\rho_{el}}\int_{\partial\Omega}\boldsymbol{n}\cdot\nabla u_p \mathrm{d}\tau = J_{\rho_{el}}\int_\Omega -\nabla^2 u_p \mathrm{d}a$$
$$= J_{\rho_{el}}\frac{\Delta p}{\eta L}hw, \qquad (22)$$

which gives the same result in 1D and in 2D. If the 1D approximation involves neglecting the entire edge region, we expect $\delta_{1D,2D} \approx 2h/w$ as seen in Fig. 3. If only the corner regions (of size λ_D) are neglected, we expect $\delta_{1D,2D} \approx 1/\tilde{h}$. From Table 3 for the 1-mM KCl solution, we expect channels #1–4 to have $\delta_{1D,2D} \lesssim 1\%$ due to $2h/w \lesssim 1\%$, channels #6–8 to have $\delta_{1D,2D} \lesssim 3\%$ due to $1/\tilde{h} \lesssim 3\%$, and channel #4 to have $\delta_{1D,2D} \approx 7\%$ due to $1/\tilde{h} \approx 7\%$. The actual values are $\delta_{1D,2D} < 2\%$. The deviations for the 10-mM borate are expected to be even lower as $\tilde{h}$ is lower, and we see that $\delta_{1D,2D} < 0.4\%$. Although for the parameters set by our experimental channels there is not a significant difference between 1D and 2D modeling, Fig. 3 shows for which parameters this in fact is the case.

4. Experimental

The theoretical model presented above is tested against streaming current and electro-osmosis experiments performed on eight different in-house fabricated silica nanochannels, with either bare or cyanosilane-coated walls, and with two different electrolytes, a 1 mM KCl solution and a 10 mM borate solution.

4.1. Device fabrication and electrolytes

We fabricated nanochannel devices in fused-silica wafers (Hoya, model 4W55-325-15C) using conventional MEMS processing techniques. The fabrication protocol was originally developed at the Stanford Nanofabrication Facility (SNF), and detailed fabrication steps and guidelines for fabricating nanochannel devices are reported elsewhere [44]. Briefly, standard photolithography was used with very short etching processes to yield channels with micrometer lateral features and nanometer depths. In this particular study, we used a reactive ion etcher to fabricate straight anisotropic channels of length $L = 20$ mm with rectangular cross

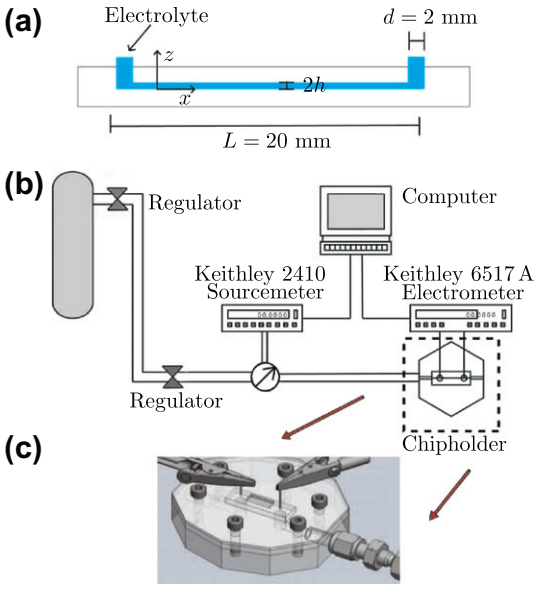

Fig. 4. (a) Side-view sketch of a nanofluidic channel used in our study. Channel lengths are typically (20 ± 1) mm, with inlet and exit diameters of 2 mm. Channel heights $2h$ vary from (38.6 ± 0.6) nm to (2032 ± 2) nm. KCl or borate buffers were the working electrolytes; channels were fabricated from fused silica, with one set coated with cyanosilane. (b) Experimental setup schematic depicting flow path of electrolyte during streaming current measurements. A high-pressure tank (rated to 6000 psi) is regulated down to the desired pressure of 8 MPa through two regulators. A sourcemeter is used in combination with a pressure transducer to electronically record pressure. A 1-fA-sensitivity electrometer is used to measure streaming currents through a custom-built chipholder. (c) Close-up sketch of the chipholder.

sections of width $w = (1.0 \pm 0.1)$ μm and with eight different heights $2h$ varying nominally from 40 nm to 2000 nm, as outlined in Table 3. Prior to bonding the channel heights $2h$ were measured using a profilometer, AFM, and/or SEM at three different locations (2 mm, 4 mm, and 6 mm) along the channel, and as verified by AFM the channels showed a roughness of less than 0.2 nm rms. Each wafer resulted in 6–12 channels at the desired height, depending on yield (50–100%). The channels were connected to two 2-mm-diameter reservoirs designed to serve as filters and support structures, as well as to minimize dead volume in the channel, Fig. 4a.

To fabricate the wafer lid, we drilled via holes in a second, fused silica wafer. To create the enclosed nanochannel device, we permanently sealed the channel wafer and lid wafer using a thermal diffusion bonding process [44]. Additionally, as also described in Ref. [14], we coated one channel from each wafer with cyano-silane (3-cyanopropyldimethylchlorosilane, Gelest, Inc.) to minimize adsorption of analyte and inhibit silica dissolution at the channel surface. The coatings were applied by filling the channels with a 1 M solution of cyano-silane in acetonitrile and leaving the solution in the channels for 12 h, which is expected to saturate the available negatively charged sites (≃25% of all silanol groups) with a neutral head group [38]. The channels were then rinsed and immersed in ethanol to prevent polymer formation during storage.

In this study, we used 1 mM KCl solutions prepared by dissolving KCl pellets (EMD chemicals) in deionized water, as well as 10 mM sodium borate buffer ($Na_2B_4O_7{\cdot}10H_2O$) prepared by dissolving NaOH pellets (Sigma, Inc.) into Borax solution (Sigma, inc), titrating until the desired pH (9.2) was achieved, and finally diluting to 10 mM. The bulk conductivity and pH of the prepared solutions were periodically measured to make sure that variations (due to temperature and humidity) did not exceed 5% of the original value. All solutions were filtered with 0.2-μm syringe filters

prior to use, (Nalgene, Inc.). Buffer exchanges were performed in a systematic fashion to avoid introducing bubbles or particulate matter into the channels.

4.2. Experimental setup

Electrical and fluidic connections to the nanochannels were made via a custom-built, high-pressure chipholder, Fig. 4b and c. Electrical connections were established by inserting silver-silver chloride (Ag/AgCl) electrodes through the top piece of the chipholder into the channel reservoirs. We soldered stainless steel tubing directly into the chipholder and established fluidic connections between the chipholder and channel reservoirs with precision O-rings (Applerubber, Inc.). A high-impedance electrometer (Keithley 6517) controlled by Labview was used to measure the streaming current (sampling frequency of 400/min) across the nanochannel. We also fabricated a home-built Faraday cage to shield the entire setup from electromagnetic radiation. We controlled the applied pressure using two high-pressure single-stage regulators that could regulate pressure between 0 and 40 MPa (≈6000 psi), and monitored the pressure with a high-precision pressure transducer (Kobold Instruments, KPK050002121). A source meter (Keithley 2410) controlled by Labview was used to both power the transducer and record the output (sampling frequency of 95/min).

4.3. Experimental procedure

Upon first use, the channel is filled with filtered deionized water via capillary action. After initial filling, the channel is examined under an epifluorescent microscope (Olympus IX70) fitted with a 40 X water immersion objective (N.A. 0.95) to ensure there are no bubbles within the channel. Then, we apply a pressure drop of 3 kPa along the channel to remove any unseen air bubbles and to achieve a stable streaming current. Once a stable current is established, the device is removed from the experimental setup, fluid from the wells is removed and the well is flushed five times with a pipettor, and the appropriate solution is placed in both wells.

Next, we perform current monitoring, following techniques of Sze [45], to determine the average experimental electro-osmotic velocity $\langle u_{eo}^{exp} \rangle$ of the system. Briefly, as in Ref. [14], one reservoir is filled with a background electrolyte with a concentration $0.9c^*$ of the target concentration c^*. Then, we raise the voltage of that well from zero to ΔV (relative to the other well that remains grounded) to allow for constant electro-osmotic flow to fill the channel with the electrolyte of concentration $0.9c^*$. After applying the voltage, the system is allowed to equilibrate for about 15 min. Finally, all liquid is removed from the well that still contains deionized water and replaced with electrolyte of concentration c^*. Voltage is applied with the opposite polarity and the current was monitored over time, as shown in Fig. 5a as the c^* concentration gradually replaces the $0.9c^*$ concentration in the nanochannel. Voltages are applied and current is monitored using a digital multimeter (Model 2410, Keithley) controlled with LabView. Platinum wires served as electrodes. Finally, $\langle u_{eo}^{exp} \rangle$ is determined as

$$\langle u_{eo}^{exp} \rangle = \frac{L}{\Delta t}, \tag{23}$$

where Δt is the time it took the c^* concentration to traverse the channel length L. Because the current monitoring procedure does not require an applied pressure gradient, and occurs in less than 1 h, we assumed negligible dissolution of the walls during this time period.

Once the channels are filled with their respective solutions and initial current measurements are taken, a pressure drop $\Delta p = 8$ MPa is applied for a period of 48 h and sampled every second, while the resulting streaming current I_p is sampled at a rate of 16,000 measurements per hour. For each channel height, we performed experiments on bare silica channels with 1 mM KCl, bare silica channels with 10 mM borate, and cyanosilane-coated channels with 10 mM borate buffer. The number of channels used per experiment varied from 1 to 4 depending on the fabrication yield. Typical raw data of $\Delta p(t)$ and $I_p(t)$ are shown in Fig. 5 for measurements on 1 mM KCl in channel #1 [panel (b–c)] and #7 [panel (d–e)], respectively. To verify that the pressure remains constant while the current increases over time, we fit the pressure and streaming current data using the expression $\Delta p(t) = (\partial \Delta p/\partial t)\ t + \Delta p(0)$ and $I_p(t) = [\partial I_p/\partial t]_{meas} t + I_p(0)$, respectively, via the build-in Matlab function *nlinfit*. Besides the fitting parameters $\partial \Delta p/\partial t$, $\Delta p(0)$, $[\partial I_p/\partial t]_{meas}$ and $I_p(0)$ the function also gives their associated uncertainties based on 95% confidence intervals. Using this information we note that for the representative cases in Fig. 5 the relative change of pressure and current over the measurement period $\Delta t = 48$ h is for channel #1

$$\frac{\partial \Delta p}{\partial t}\frac{\Delta t}{\Delta p(0)} = (0.2 \pm 0.2) \times 10^{-4}, \tag{24a}$$

$$\left[\frac{\partial I_p}{\partial t}\right]_{meas}\frac{\Delta t}{I_p(0)} = (153.4 \pm 1.0) \times 10^{-4}, \tag{24b}$$

and for channel #7

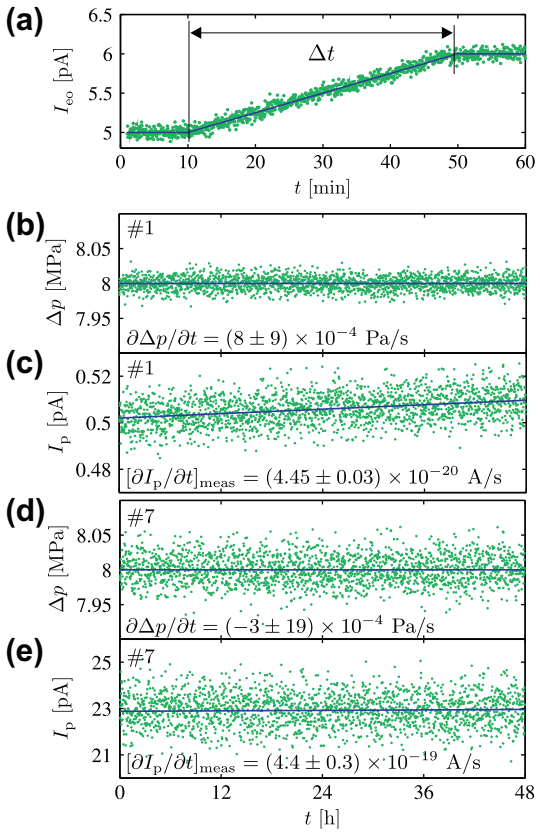

Fig. 5. (a) Typical raw data (green points) from an electro-osmotic flow filling experiment showing the current I_{eo} versus time t, as well as fitting lines (blue). (b) Measured applied pressure drop Δp (green points) versus time over a 48-h time period for 1 mM KCl solution (pH 5.6 and $\lambda_D = 10$ nm) in channel #1 (for clarity only ~2000 out of 172,800 data points are shown). Also shown is the fitting line (blue) from which the slope $\partial \Delta p/\partial t$ with associated uncertainty is determined. (c) The measured streaming current I_p (green points) resulting from the applied pressure drop in panel (b) versus time (for clarity only ~2000 out of 768,000 data points are shown). From the fitting line (blue), the slope $[\partial I_p/\partial t]_{meas}$ and initial current $I_p(0)$ with associated uncertainties are determined. (d–e) The same as panels (b) and (c) but for channel #7. (For interpretation of the references to color in this figure legend, the reader is referred to the web version of this article.)

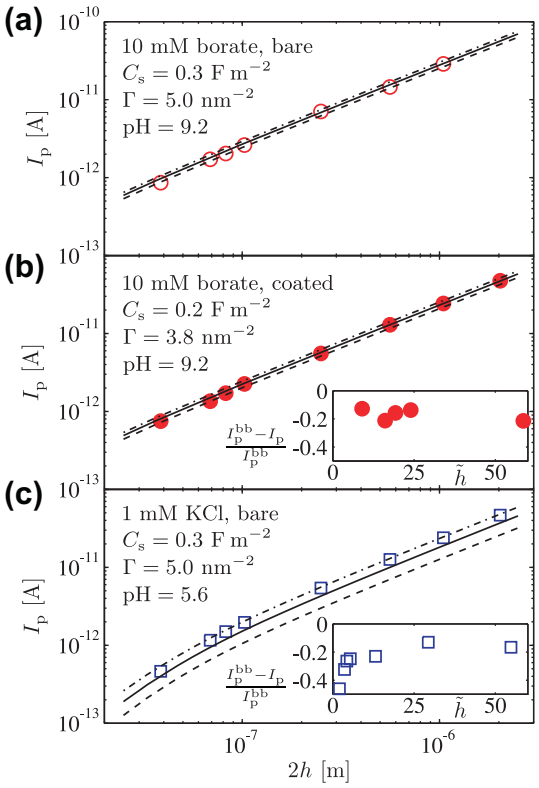

Fig. 6. Log–log plots of measured (symbols) and predicted (full lines, 2D model with pK = 6.6) streaming current I_p versus channel height $2h$ for: (a) 10 mM borate in bare channels (open red circles), (b) 10 mM borate in cyanosilane coated channels (filled red circles), and (c) 1 mM KCl in bare channels (open blue squares). Estimated theoretical error bounds are found using pK = 6.0 (dash-dotted lines) and pK = 7.2 (dashed lines). The relative experimental error is negligible, of order 10^{-4} as discussed in Section 4.3, and therefore undiscernable in the plot. The insets of panel (b) and (c) show the relative deviation of the same experimental data I_p from those of the 10 mM borate bare silica channel, I_p^{bb}. (For interpretation of the references to color in this figure legend, the reader is referred to the web version of this article.)

$$\frac{\partial \Delta p}{\partial t}\frac{\Delta t}{\Delta p(0)} = (-0.1 \pm 0.4) \times 10^{-4}, \tag{25a}$$

$$\left[\frac{\partial I_p}{\partial t}\right]_{meas}\frac{\Delta t}{I_p(0)} = (33.1 \pm 2.3) \times 10^{-4}, \tag{25b}$$

Hence, since the relative change in the current is two to three orders of magnitude larger than that of the pressure, we rule out that any systematic change in $\Delta p(t)$ could be responsible for the rise in $I_p(t)$.

Finally, we take the streaming current for a given experimental condition to be $I_p = I_p(0)$ in the aforementioned fit as the channels have their nominal height at $t = 0$. The experimental uncertainty, from e.g. pressure fluctuations and noise from the electrometer, can then be estimated from the 95% confidence interval half-width $\Delta I_p(0)$. For the experimental conditions in Fig. 5, the relative uncertainty $\Delta I_p(0)/I_p(0)$ of the streaming current is $\sim 5 \times 10^{-5}$ for channel #1 and $\sim 1 \times 10^{-4}$ for channel #7. In Fig. 6 we plot I_p versus height h for three different cases. The experimental uncertainty $\Delta I_p(0)/I_p(0)$ of order $\sim 10^{-4}$ is negligible in comparison to the uncertainty from the 10% variation in the surface pK-value, which is indicated by the non-solid curves.

5. Results and discussion

5.1. The electro-osmotic velocity

Using the procedure described in Section 4.3, the average electro-osmotic flow velocity $\langle u_{eo}^{exp} \rangle$, Eq. (23), was determined for the tallest nanochannel, #8 in Table 3, for bare silica walls with 1 mM KCl and with 10 mM borate, and for coated silica walls with 10 mM borate. The theoretically predicted electro-osmotic flow velocity $\langle u_{eo}^{thr} \rangle$ was determined using Eq. (19a), and the results including uncertainties are

1 mM KCl, bare

$$\langle u_{eo}^{exp} \rangle = (7.0 \pm 0.4)\ \frac{\mu m}{s}, \quad \langle u_{eo}^{thr} \rangle = (5.6 \pm 1.8)\ \frac{\mu m}{s}, \tag{26a}$$

10 mM borate, bare

$$\langle u_{eo}^{exp} \rangle = (8.3 \pm 0.4)\ \frac{\mu m}{s}, \quad \langle u_{eo}^{thr} \rangle = (8.4 \pm 0.8)\ \frac{\mu m}{s}, \tag{26b}$$

10 mM borate, coated

$$\langle u_{eo}^{exp} \rangle = (7.0 \pm 0.4)\ \frac{\mu m}{s}, \quad \langle u_{eo}^{thr} \rangle = (7.0 \pm 0.7)\ \frac{\mu m}{s}. \tag{26c}$$

In all three cases, the agreement between theory and experiment is good and within the given experimental and theoretical uncertainties. The relative deviations are of the order of 10%. The theoretical uncertainties are dominated by the assignment of pK as shown in Table 2, while the experimental ones are mainly due to the width measurements, see Table 2. The theoretical values are based on the full 2D model and account for relative deviations of u_{eo} from the flat-wall value, as shown in Fig. 3b

5.2. The streaming current

Results for the streaming current are shown in Fig. 6 as log-log plots of measurements (symbols) and theoretical predictions (full black curve, 2D model) of streaming current I_p versus channel height $2h$ for the three different conditions tested: 1 mM KCl in bare channels (open red circles), 10 mM borate in bare channels (filled red circles), and 10 mM borate buffer in cyanosilane-coated channels (open blue squares). There are no adjustable parameters, and the agreement between theory and experiment is good, within 10%.

We find that the two parameters that have the largest influence on the uncertainty in the 2D modeling are the channel width and the surface pK-value. In Table 3 is given an estimate of the error in the width of the channel of 10%. An equivalent 10% uncertainty in the pK-value is estimated based on literature values [42,25,31,43,27,29]. We find that of the two parameters the pK-value (pK = 6.6 ± 0.6, Table 2) dominates the resulting uncertainty in the 2D model. We therefore find the error bounds by calculating I_p using pK = 6.0 (dash-dotted lines) and *7.2* (dashed lines), respectively. For the experimental uncertainty, and as discussed in Section 4.3, the 95% confidence interval half-width $\Delta I_p(0)$ for the fitted streaming current $I_p = I_p(0)$ typically yield a relative uncertainty $\Delta I_p(0)/I_p(0) \sim 10^{-4}$, which is negligible in comparison with that from the pK-variation discussed earlier and not discernable in Fig. 6. Finally, based on the above uncertainties, we see from Fig. 6 that the measured data points lie within the error curves.

The insets of Fig. 6b and c show the experimental data plotted relative to the data from borate in bare channels. These plots highlight the behavior of our systems with coated channels as well as with a lower concentration buffer. First, it can be seen that the streaming current decreases by about 20% when the number of available surface sites is reduced by surface coating, going from 10 mM bare borate ($\Gamma = 5.0$ nm^{-2}) to the 10 mM coated borate ($\Gamma = 3.8$ nm^{-2}). This reduction in streaming current is fairly constant across channel heights, which is consistent with the assumption that only the surface charge density is different. However, when comparing the streaming current from the 10 mM bare borate channel to the 1 mM bare KCl channel, we note that the streaming current reduction is larger at lower channel heights. This is due to the fact that the double layers are strongly overlapping in

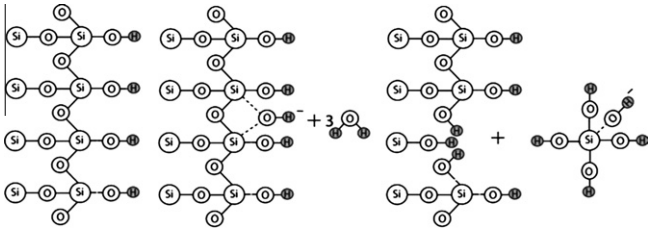

Fig. 7. One proposed mechanism for silica dissolution presented in, and image adapted from, Ref. [46].

this regime (whereas with 10 mM borate the double layers are still non-overlapping), which clearly reduces the streaming current.

Having verified the accuracy of the model for the forward problem, i.e., predicting streaming currents in the nanochannels of interest, we next turn to the inverse problem of estimating dissolution rates given extended time-sensitive streaming current measurements.

5.3. Method for determining dissolution rates

In geological systems, it has been found that saline solutions flowing through porous silicates dissolve the solid matrix at a rate of approximately 0.01 mg/m^2/h [46]. Given that the density of fused silica is 2203 kg/m^3, we obtain

$$1\ \frac{\mathrm{mg}}{\mathrm{m^2 h}} \sim 0.4539\ \frac{\mathrm{nm}}{\mathrm{h}} = 1.26\times 10^{-13}\ \frac{\mathrm{m}}{\mathrm{s}}, \tag{27a}$$

or conversely

$$1\ \frac{\mathrm{m}}{\mathrm{s}} = 7.93\times 10^{12}\ \frac{\mathrm{mg}}{\mathrm{m^2 h}}. \tag{27b}$$

The mechanism of silica dissolution is complex and not yet well understood, but one mechanism for the dissolution discussed in the literature [46] is shown in Fig. 7.

Here, we propose a method for determining dissolution rates under controlled experimental conditions using our model and experimental data. Referring back to Fig. 5b and c, we note that although the applied pressure drop remains constant over a period of 48 h, the streaming current steadily rises. This fact, together with the following three assumptions, forms the basis of the method: (*i*) all changes in current are due solely to dissolution of the wall, aided by the continuous renewal of fresh buffer by the axial flow; (*ii*) ionized silanol radicals are few and highly unstable and thus do not contribute to the current; (*iii*) spatial variations in the dissolution rate are averaged out over the entire surface of the channel.

To calculate dissolution rates, we use Eq. (14b) to obtain a numerical estimate for the change δI_p in the streaming current as a function of the change $\delta A = 2(w+h)\,\delta\ell$ in the cross-sectional area A, in terms of the (small) thickness $\delta\ell$ of the dissolved layer,

$$\left[\frac{\partial I_\mathrm{p}}{\partial \ell}\right]_\mathrm{calc} = \frac{\partial I_\mathrm{p}}{\partial A}\frac{\partial A}{\partial \ell} \approx \frac{1}{\delta\ell}\left[I_\mathrm{p}(A+\delta A) - I_\mathrm{p}(A)\right], \tag{28}$$

where we choose $\delta\ell = 0.01h$. Combining this with the experimentally measured rate of change $[\partial I_\mathrm{p}/\partial t]_\mathrm{meas}$ of the streaming current, Fig. 5c, yields the dissolution rate dm/dt per unit area (in units of mg/m^2/h) as,

$$\frac{\mathrm{d}m}{\mathrm{d}t} = 7.93\times 10^{12}\ \frac{\mathrm{mg}}{\mathrm{m^2 h}}\ \frac{\mathrm{s}}{\mathrm{m}} \times \left[\frac{\partial I_\mathrm{p}}{\partial t}\right]_\mathrm{meas} \times \left[\frac{\partial I_\mathrm{p}}{\partial \ell}\right]^{-1}_\mathrm{calc}. \tag{29}$$

In the Supplementary information, we list the numerical values of $[\partial I_\mathrm{p}/\partial t]_\mathrm{meas}$, $[\partial I_\mathrm{p}/\partial l]_\mathrm{calc}$, and d$m$/d$t$ for each experimental condition.

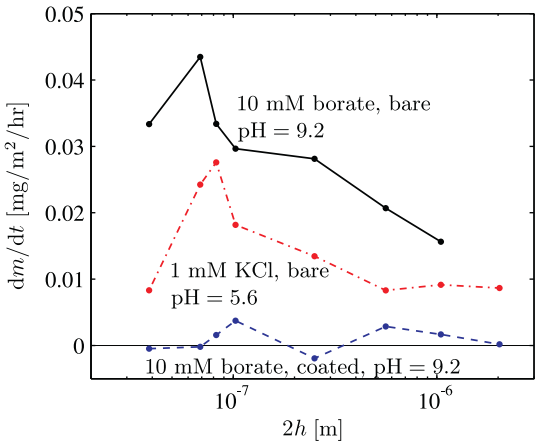

Fig. 8. Predicted silica dissolution rate dm/dt vs. channel height 2h based, via Eq. (29), on measured $[\partial I_\mathrm{p}/\partial t]_\mathrm{meas}$ and calculated $[\partial I_\mathrm{p}/\partial l]_\mathrm{calc}$ (numerical values are given in the Supplementary information). The three curves are for: 1 mM KCl in bare channel (dash-dotted red curve), 10 mM borate in bare channel (full black curve), and 10 mM borate in cyanosilane-coated channel (dashed blue curve). (For interpretation of the references to color in this figure legend, the reader is referred to the web version of this article.)

The theoretically predicted dissolution rates based on measured $[\partial I_\mathrm{p}/\partial t]_\mathrm{meas}$ for our experimental nanochannel system are shown in Fig. 8. We note that the estimated rates are on the same order of magnitude as previous results in the field of geological systems [46], which allows us to believe that our method is viable for silica dissolution studies. Furthermore, also in agreement with earlier findings [9], the dissolution rate increases as pH and ionic strength increase going from 1 mM KCl (pH 5.6) to 10 mM borate (pH 9.2) in bare silica channels. Other studies have pointed out that electric double-layer interaction in un-confined geometries increases the dissolution rates [9]. This we also see in our calculations, as the dissolution rate increases when the double layers start to overlap as the channel half-height h is decreased. A final point that corroborates our model is the prediction of a negligible dissolution rate (fluctuates around zero) for the cyanosilane-coated channel, a well-known feature from other studies [38,47,48].

On top of this, we can use our model for novel studies of silica dissolution, for example the influence of extreme confinement. From Fig. 8 we note that the increase in dissolution rate starts earlier for 1 mM KCl than 10 mM borate as channel height decreases, indicating that this may be due to electric double layer effects. However, because the peak is roughly at the same height for both cases, diffusion-limited dissolution may be the dominating physics at small channel heights. This is in line with a common viewpoint about dissolution, which holds that charges such as OH^- near the wall catalyze de-polymerization and that the newly dissolved silanol radicals diffuse away from the surface.

In general, using our method of hours-long streaming current measurements will enable systematic studies of the mechanism underlying dissolution of silica in a number of controlled experiments: The channel geometry can be varied from the case of thin non-overlapping double layers in very tall microchannels to that of strongly overlapping double layers at extreme confinement in very shallow nanochannels. Diffusion limited dissolution rates and the effect of continuous renewal of buffer can be studied through varying the imposed pressure-driven electrolyte flow. The chemical conditions can be varied through the detailed composition and ionic strength of the buffer as well as the coating conditions of the surface. The small size of micro- and nanofluidic systems facilitates accurate temperature control. These advantages suggest that our method may be useful for future studies of silica dissolution.

6. Conclusion

We have advanced the capabilities of our chemical-equilibrium electrokinetic model to account for pressure-driven flows and full 2D cross-sectional geometries without adjustable parameters. These advances have been validated against experimental results on eight bare and cyanosilane-coated silica nanochannels of heights between 40 nm and 2000 nm for 1 mM KCl solutions and 10 mM borate buffers. Numerical predictions, based on a finite-element-method implementation of our model, of the electro-osmotic velocities and streaming currents exhibit good agreement with measured data, and we have determined when the 2D model is necessary to employ. Finally, by combining model predictions with measurements over 48 h of the streaming currents, we have developed a method to estimate the dissolution rate of the silica walls, typically around 0.01 mg/m^2/h, under controlled experimental conditions.

Appendix A. Supplementary material

Supplementary data associated with this article can be found, in the online version, at doi:10.1016/j.jcis.2011.04.011.

References

[1] R. Schoch, J. Han, P. Renaud, Rev. Mod. Phys. 80 (3) (2008) 839–883.
[2] W. Sparreboom, A. van den Berg, J.C.T. Eijkel, Nat. Nanotechnol. 4 (11) (2009) 713–720.
[3] L. Bocquet, E. Charlaix, Chem. Soc. Rev. 39 (3) (2010) 1073–1095.
[4] M. Napoli, J.C.T. Eijkel, S. Pennathur, Lab. Chip. 10 (8) (2010) 957–985.
[5] W. Sparreboom, A. van den Berg, J.C.T. Eijkel, New J. Phys. 12 (1) (2010) 015004.
[6] P.M. Dove, Geochim. Cosmochim. Acta 63 (22) (1999) 3715–3727.
[7] P.M. Dove, N. Han, J.J.D. Yoreo, Proc. Natl. Acad. Sci. 102 (43) (2005) 15357–15362.
[8] P.M. Dove, N. Han, A.F. Wallace, J.J.D. Yoreo, Proc. Natl. Acad. Sci. 105 (29) (2008) 9903–9908.
[9] G.W. Greene, K. Kristiansen, E.E. Meyer, J.R. Boles, J.N. Israelachvili, Geochim. Cosmochim. Acta 73 (10) (2009) 2862–2874.
[10] N.R. Tas, J.W. Berenschot, P. Mela, H.V. Jansen, M. Elwenspoek, A. van den Berg, Nano Letters 2 (9) (2002) 1031–1032.
[11] Q. Xia, K.J. Morton, R.H. Austin, S.Y. Chou, Nano Letters 8 (11) (2008) 3830–3833.
[12] Y. Zhao, E. Berenschot, H. Jansen, N. Tas, J. Huskens, M. Elwenspoek, Microelectron. Eng. 86 (4–6) (2009) 832–835.
[13] S. Nam, M. Lee, S. Lee, D. Lee, S.M. Rossnagel, K. Kim, Nano Letters 10 (9) (2010) 3324–3329.
[14] M.B. Andersen, J. Frey, S. Pennathur, H. Bruus, J. Colloid Interface Sci. 353 (2011) 301–310.
[15] J. Yang, F. Lu, L.W. Kostiuk, D.Y. Kwok, J. Micromech. Microeng. 13 (6) (2003) 963–970.
[16] O. El-Gholabzouri, M.A. Cabrerizo, R. Hidalgo-Álvarez, J. Colloid Interface Sci. 214 (2) (1999) 243–250.
[17] S. Alkafeef, R.J. Gochin, A.L. Smith, Colloid Surface A 195 (1–3) (2001) 77–80.
[18] C. Fritzmann, J. Löwenberg, T. Wintgens, T. Melin, Desalination 216 (1–3) (2007) 1–76.
[19] M.A. Shannon, P.W. Bohn, M. Elimelech, J.G. Georgiadis, B.J. Marinas, A.M. Mayes, Nature 452 (7185) (2008) 301–310.
[20] P.M. Biesheuvel, M.Z. Bazant, Phys. Rev. E 81 (3) (2010) 031502.
[21] F. van der Heyden, D. Stein, C. Dekker, Phys. Rev. Lett. 95 (11) (2005) 116104.
[22] F.H.J. van der Heyden, D.J. Bonthuis, D. Stein, C. Meyer, C. Dekker, Nano Letters 6 (10) (2006) 2232–2237.
[23] F.H.J. van der Heyden, D. Stein, K. Besteman, S.G. Lemay, C. Dekker, Phys. Rev. Lett. 96 (22) (2006) 224502.
[24] F.H.J. van der Heyden, D.J. Bonthuis, D. Stein, C. Meyer, C. Dekker, Nano Letters 7 (4) (2007) 1022–1025.
[25] S.H. Behrens, D.G. Grier, J. Chem. Phys. 115 (14) (2001) 6716–6721.
[26] P.M. Biesheuvel, J. Colloid Interface Sci. 275 (2) (2004) 514–522.
[27] M. Wang, A. Revil, J. Colloid Interface Sci. 343 (1) (2010) 81–386.
[28] C. Duan, A. Majumdar, Nat. Nanotechnol. 5 (12) (2010) 848–852.
[29] K.L. Jensen, J.T. Kristensen, A.M. Crumrine, M.B. Andersen, H. Bruus, S. Pennathur, Phys. Rev. E 83, 056307 (2011).
[30] D.Y. Chan, T.W. Healy, T. Supasiti, S. Usui, J. Colloid Interface Sci. 296 (1) (2006) 50–158.
[31] K.G.H. Janssen, H.T. Hoang, J. Floris, J. de Vries, N.R. Tas, J.C.T. Eijkel, T. Hankemeier, Anal. Chem. 80 (21) (2008) 8095–8101.
[32] R.F. Probstein, Physicochemical Hydrodynamics: An Introduction, Wiley-Interscience, 1994.
[33] N.L. Burns, J. Colloid Interface Sci. 183 (1) (1996) 249–259.
[34] M.Z. Bazant, M.S. Kilic, B.D. Storey, A. Ajdari, Adv. Colloid Interface Sci. 152 (1–2) (2009) 48–88.
[35] R.E.G. van Hal, J.C.T. Eijkel, P. Bergveld, Adv. Colloid Interface Sci. 69 (1–3) (1996) 31–62.
[36] D.E. Yates, S. Levine, T.W. Healy, J. Chem. Soc., Faraday Trans. 1 (70) (1974) 807–1818.
[37] J.A. Davis, R.O. James, J.O. Leckie, J. Colloid Interface Sci. 63 (3) (1978) 480–499.
[38] R.J. White, E.N. Ervin, T. Yang, X. Chen, S. Daniel, P.S. Cremer, H.S. White, J. Am. Chem. Soc. 129 (38) (2007) 1766–11775.
[39] A. Persat, R.D. Chambers, J.G. Santiago, Lab. Chip. 9 (17) (2009) 2437.
[40] A. Persat, R.D. Chambers, J.G. Santiago, Buffer calculator, 2010. <http://microfluidics.stanford.edu/download>.
[41] A. Persat, M.E. Suss, J.G. Santiago, Lab. Chip. 9 (17) (2009) 2454.
[42] P. Schindler, H.R. Kamber, Helv. Chim. Acta 51 (7) (1968) 781–1786.
[43] R.B.H. Veenhuis, E.J. van der Wouden, J.W. van Nieuwkasteele, A. van den Berg, J.C.T. Eijkel, Lab. Chip. 9 (24) (2009) 3472–3480.
[44] S. Pennathur, J.G. Santiago, Anal. Chem. 77 (21) (2005) 6782–6789.
[45] A. Sze, D. Erickson, L. Ren, D. Li, Zeta-potential measurement using the smoluchowski equation and the slope of the current-time relationship in electroosmotic flow, J. Colloid Interface Sci. 261 (2) (2003) 402–410.
[46] R.K. Iler, The Chemistry of Silica: Solubility, Polymerization, Colloid and Surface Properties, and Biochemistry, Wiley, New York, 1979.
[47] S. Prakash, T.M. Long, J.C. Selby, J.S. Moore, M.A. Shannon, Anal. Chem. 79 (4) (2007) 1661–1667.
[48] S. Prakash, M. Karacor, S. Banerjee, Surf. Sci. Rep. 64 (7) (2009) 233–254.